Volume 8
Number 13
7 July 2024
Pages 2791–2992

Sustainable Energy & Fuels

Interdisciplinary research for the development of sustainable energy technologies

rsc.li/sustainable-energy

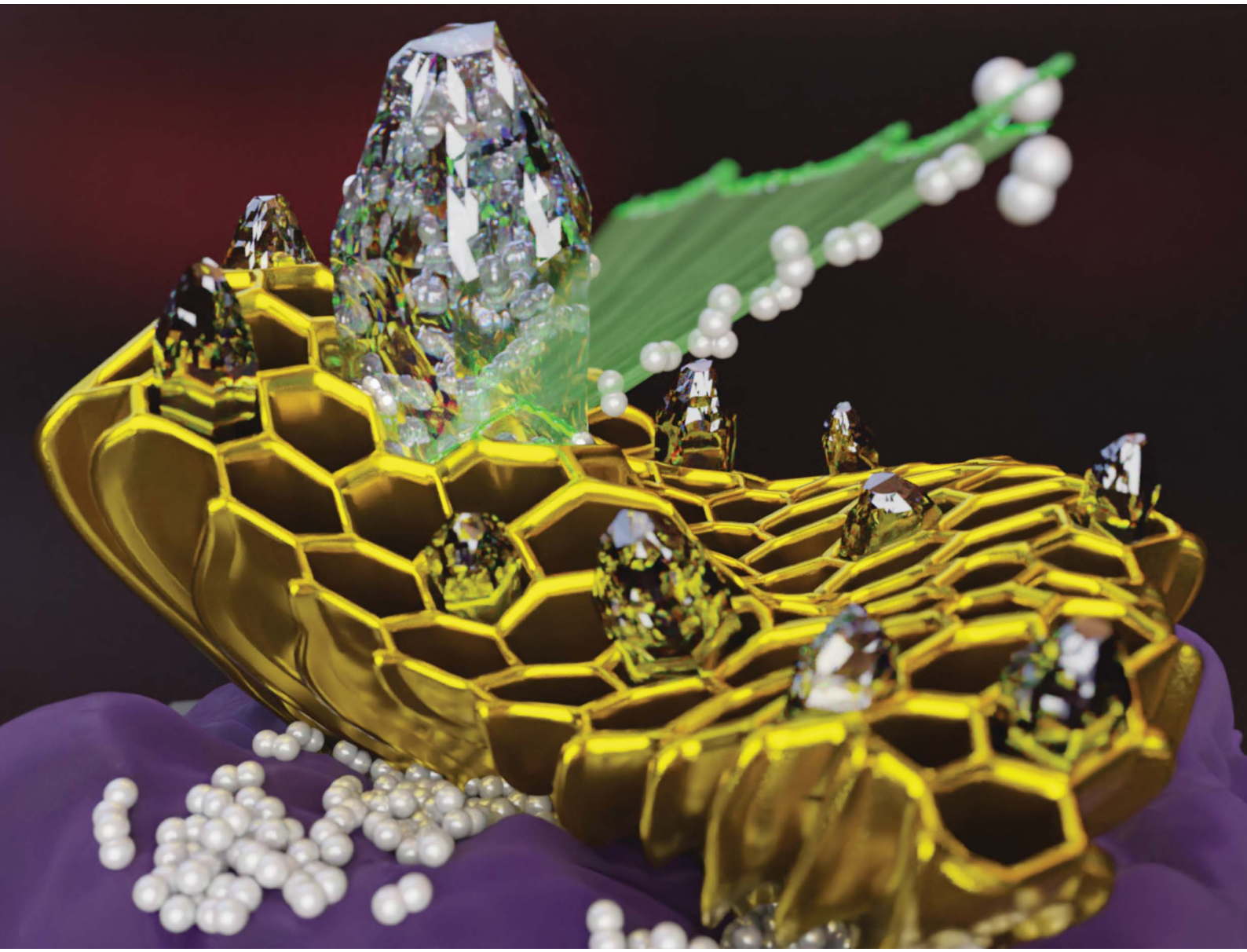

ISSN 2398-4902

ROYAL SOCIETY OF CHEMISTRY

PAPER

Eric Breynaert *et al.*

Surface modification of mesostructured cellular foam to enhance hydrogen storage in binary THF/H_2 clathrate hydrate

Sustainable Energy & Fuels

ROYAL SOCIETY OF CHEMISTRY

PAPER

View Article Online
View Journal | View Issue

Cite this: *Sustainable Energy Fuels*, 2024, **8**, 2824

Surface modification of mesostructured cellular foam to enhance hydrogen storage in binary THF/H_2 clathrate hydrate†

Nithin B. Kummamuru,[ab] Radu-George Ciocarlan,[c] Maarten Houlleberghs,[d] Johan Martens,[de] Eric Breynaert,[*de] Sammy W. Verbruggen,[af] Pegie Cool[c] and Patrice Perreault[*bg]

This study introduces solid-state tuning of a mesostructured cellular foam (MCF) to enhance hydrogen (H_2) storage in clathrate hydrates. Grafting of promoter-like molecules (*e.g.*, tetrahydrofuran) at the internal surface of the MCF resulted in a substantial improvement in the kinetics of formation of binary H_2-THF clathrate hydrate. Identification of the confined hydrate as sII clathrate hydrate and enclathration of H_2 in its small cages was performed using XRD and high-pressure ^{1}H NMR spectroscopy respectively. Experimental findings show that modified MCF materials exhibit a ~1.3 times higher H_2 storage capacity as compared to non-modified MCF under the same conditions (7 MPa, 265 K, 100% pore volume saturation with a 5.56 mol% THF solution). The enhancement in H_2 storage is attributed to the hydrophobicity originating from grafting organic molecules onto pristine MCF, thereby influencing water interactions and fostering an environment conducive to H_2 enclathration. Gas uptake curves indicate an optimal tuning point for higher H_2 storage, favoring a lower density of carbon per nm^2. Furthermore, a direct correlation emerges between higher driving forces and increased H_2 storage capacity, culminating at 0.52 wt% (46.77 mmoles of H_2 per mole of H_2O and 39.78% water-to-hydrate conversions) at 262 K for the modified MCF material with fewer carbons per nm^2. Notably, the substantial H_2 storage capacity achieved without energy-intensive processes underscores solid-state tuning's potential for H_2 storage in the synthesized hydrates. This study evaluated two distinct kinetic models to describe hydrate growth in MCF. The multistage kinetic model showed better predictive capabilities for experimental data and maintained a low average absolute deviation. This research provides valuable insights into augmenting H_2 storage capabilities and holds promising implications for future advancements.

Received 22nd January 2024
Accepted 12th April 2024

DOI: 10.1039/d4se00114a

rsc.li/sustainable-energy

1. Introduction

2022 was a critical year for the European Union, both in terms of changing the traditional energy import routes and hastening its energy transition towards low-emission alternative fuels. This complements the recommendation of the 27th United Nations Climate Change Conference to prioritize decarbonization.[1] Hydrogen (H_2) is a clean energy carrier with a >200% higher energy density than methane (CH_4) (H_2 ~120 MJ Kg^{-1}; CH_4: ~50 MJ Kg^{-1}). With a predicted global H_2 demand of 95 million tonnes by 2030, H_2 is considered to be a crucial pillar of the future energy system, especially for industrial sectors.[2,3] Despite H_2's potential, its safety and processability (*i.e.* storage and transportation) remain major challenges limiting the development of novel H_2 technologies and delaying the deployment of an H_2 economy.[4] Chemi- and physi-sorption based H_2 storage has often been touted as an alternative to conventional storage of molecular H_2 in high-pressure tanks or *via* liquefaction, which comes with a variety of drawbacks.[5,6] While sorption based storage can exhibit superior gravimetric and/or volumetric H_2 storage densities, many materials potentially exceed the DOE target of 5.6 wt% H_2 for mobile applications.[7–9] H_2 release is often energy intensive and not fully reversible. To confront slow kinetics, poor reversibility, cycling instability, and

[a]*Sustainable Energy Air & Water Technology (DuEL), Department of Bioscience Engineering, University of Antwerp, Groenenborgerlaan 171, 2020 Antwerpen, Belgium*
[b]*Laboratory for the Electrification of Chemical Processes and Hydrogen (ElectrifHy), University of Antwerp, Olieweg 97, 2020 Antwerp, Belgium. E-mail: Patrice.perreault@uantwerpen.be*
[c]*Department of Chemistry, University of Antwerp, Universiteitsplein 1, 2610 Wilrijk, Belgium*
[d]*KU Leuven, Centre for Surface Chemistry and Catalysis-Characterization and Application Team (COK-KAT), Celestijnenlaan 200F – Box 2461, Leuven 3001, Belgium. E-mail: eric.breynaert@kuleuven.be*
[e]*NMR/X-Ray Platform for Convergence Research (NMRCoRe), Celestijnenlaan 200F – Box 2461, Leuven 3001, Belgium*
[f]*NANOlab Center of Excellence, University of Antwerp, Groenenborgerlaan 171, 2020 Antwerpen, Belgium*
[g]*University of Antwerp, BlueApp, Olieweg 97, 2020 Antwerpen, Belgium*

† Electronic supplementary information (ESI) available. See DOI: https://doi.org/10.1039/d4se00114a

thermal management issues, substantial R&D resources are committed to the field of materials science.[6,10]

Gas hydrates or clathrate hydrates are crystalline materials formed under favorable thermodynamic conditions when suitable guest (H_2 in this work) molecules are incorporated in the cages of 3-dimensional hydrogen bonded solid water (H_2O) structures.[11] Because of its renewable and environmentally friendly nature as the principal storage medium is H_2O, clathrate based H_2 storage technology has regained significant momentum.[12,13] Minimal temperature or pressure swings outside the hydrate stability zone enable swift recovery of the stored molecular H_2 without losing H_2O or promoter molecules.[14–16] Recently, gas recovery from clathrate hydrate was even demonstrated without melting the solid water phase, further improving the energy balance of the process.[17] Pure H_2 clathrates entered the focus of attention when Mao *et al.*[15] reported that classical sII hydrate structures allow to encapsulate respectively two and four hydrogen molecules in each of its sixteen dodecahedra (small) and eight hexakaidecahedron (large) cages. In this scheme, complete occupancy would deliver a total H_2 storage capacity of 5 wt%. Neutron diffraction analysis by Lokshin *et al.*,[18] however, refuted the claims of double occupancy of H_2 in small cages. Regardless of this occupancy debate, the exceedingly high pressures (between 0.75 and 3.1 GPa) required to stabilize pure H_2 clathrate hydrate in the bulk remain a major factor limiting deployment of bulk H_2 clathrate hydrate in H_2 storage and transportation applications. To resolve this aspect and make H_2 clathrates industrially viable, binary clathrate hydrates incorporating both H_2 and promoter molecules have been put forward.[13]

Stoichiometric concentrations of thermodynamic promoters (*e.g.* tetrahydrofuran (THF); 5.56 mol%) can stabilize binary promoter-gas sII clathrate hydrate structures at pressures as low as 5 MPa and 279.6 K, albeit at the expense of storage capacity for the gas.[12,13,16,19,20] Promoter molecules typically occupy a significant fraction of larger clathrate cages, indeed leaving mostly only small cages open for gas enclathration. In an attempt to enable a higher H_2 storage density, various studies have proposed strategies for reducing the concentrations of these thermodynamic promoters below the stoichiometric concentration.[21–24] These strategies were, however, contested by claims that the H_2 storage capacity at reduced pressure and elevated temperature is dependent on the promoter concentration. Optimization of the promoter concentration would therefore not allow the storage capacity to be enhanced.[25–28]

While much attention has been focused on cage occupancies and determining overall H_2 storage capacities with different thermodynamic promoters (THF being cited as the best promoter thus far),[13,19,29] the constraints on enclathration kinetics and the mass transfer rate have largely been overlooked, causing further impediments to foster this technology. While mechanical mixing can potentially assist in enhancing its kinetics, gas enclathration is typically a slow process due to insufficient contact between gas and liquid phases[27,30,31] (in this case between H_2 and H_2O + promoter molecules). Mixing on top is an energy-intensive operation as the viscosity of the system increases with increasing conversion.[32–34] As an alternative to mechanical mixing of the bulk gas–liquid system, pre-synthesized pure promoter molecules, including THF, have been made to come into contact with H_2 gas at high-pressure to convert the pure promoter-molecule clathrate hydrate into binary clathrate hydrate. Melting of the binary clathrate hydrate to a liquid phase upon gas release however renders this strategy unsuitable for continuous cycles.[27,35–38] Enhancing the kinetics of synthesizing a binary H_2 hydrate from a bulk aqueous phase under mild thermodynamic conditions in a process incorporating recycling of the H_2O and promoter molecules therefore remains a major challenge.

A limited number of publications report the option to accelerate the kinetics of binary clathrate hydrate formation by incorporating porous materials in an unstirred reactor.[25,35,39–45] This paves the way for further research on quiescent and porous systems that could propel clathrate-based H_2 technology to new frontiers. While the literature clearly demonstrates enhanced growth of clathrate hydrate with increasing the surface-to-volume ratio, the process is affected by multiple factors including surface chemistry, pore morphology, and wettability.[27,30] Pore size and network morphology not only affect the gas–liquid contact, but together with the surface chemistry of the pores, they also profoundly impact the local organization of H_2O,[46] thereby directly affecting clathrate hydrate nucleation. Molecular simulations by Bai *et al.*[47] also show that gas hydrate nucleation occurs more easily on less hydrophilic surfaces. This is supported experimentally by J. Wang *et al.*[48] who reported the induction time of gas clathrate hydrate formation to be more than 8 times shorter in hydrophobic materials than in hydrophilic materials. Hydrophobic nano-confinement indeed induces a reorganization of the hydrogen bonding structure of H_2O, towards a more ice-like tetrahedrally bonded organization which appears to promote clathrate hydrate nucleation.[39,42,46,49–60]

Given the advantages of hydrophobic surfaces in gas hydrate nucleation, the present work attempts to design and synthesize porous materials enabling the enclathration kinetics of binary H_2 clathrate hydrates to be boosted. Consequently, this study focuses on silica-based mesoporous materials that have been comprehensively designed in terms of pore networks and with pore diameters exceeding 17.3 Å.[11] Such pore size should allow the accommodation of an sII clathrate hydrate unit cell, while functionalization with a promoter molecule (THF) could assist in stabilizing H_2 clathrate hydrate and potentially allow its concentration in the aqueous phase to be reduced. The chosen silica material, specifically mesostructured cellular foam (MCF), offers several advantages due to its relatively large pores in the mesoporous region, which, in turn, facilitate network accessibility. As THF today still is the best promoter molecule for binary H_2 clathrate hydrate formation, the MCF pore surface was functionalized with tetrahydro furfuryloxypropyl triethoxysilane, a THF-like molecule that can be grafted on silica surfaces while retaining high mobility due to its long ether chain. To evaluate if the grafted THF-like molecules assist in perturbing the H_2O structure and lowering the nucleation barrier, binary H_2-THF clathrate hydrate formation was studied as a function of temperature (268 K, 265 K, and 262 K; 7 MPa

initial pressure) in grafted and pristine MCF foams, evaluating kinetics as well as H_2 storage capacity.

2. Experimental methods

2.1. Materials

Table 1 lists all the chemicals used in this work and all of them were used without any purification. H_2 (99.99% purity) was supplied by Air Liquide Benelux Industries and for the liquid phase deionized H_2O was used.

2.2. Synthesis and characterization methods

The MCF silica material was synthesized *via* a previously reported template approach.[61] In a typical experimental procedure, the triblock copolymer P123 ($EO_{20}PO_{70}EO_{20}$) surfactant was dissolved in a solution of HCl acidified H_2O and stirred overnight. Next, appropriate amounts of etching agent ammonium fluoride (NH_4F) and swelling agent 1, 3, 5-trimethylbenzene (mesitylene) were added and the mixture was equilibrated at 308–313 K for 1 h while stirring. Next, tetraethylorthosilicate (TEOS) was added dropwise to the stirred solution over a timeframe of 30 minutes (approximately 1 mL min^{-1}). Subsequently, the newly formed white precipitate was aged at 313 K for 20 h while stirring. The synthesis was finalized by transferring the white precipitate to an autoclave and subjecting it to hydrothermal treatment for 24 h at 373 K. Afterwards, the solid was recovered by filtering, subsequently rinsed with distilled H_2O, and then dried. The molar ratio of the precursors used in the synthesis was as follows: 1 TEOS: 5.87 HCl: 194 H_2O: 0.017 P123: 0.031 NH_4F: 0.815 1, 3, 5-trymethilbenzene. Before using it in the subsequent experiments, the dry material was calcined at 550 °C for 6 hours, raising the temperature from 295 to 823 K at 1 K per minute. The resulting product was denoted as MCF (n-f) and will be referred to as such throughout this manuscript.

After the synthesis, the MCF silica material underwent surface modification using tetrahydro furfuryloxypropyl triethoxysilane, drawing inspiration from a previously documented approach.[62] Prior to the procedure, each batch of 1.2 g of the MCF material was subjected to overnight drying at 473 K under atmospheric pressure. Subsequently the dried batches were introduced in a glovebox under an argon atmosphere and each batch was suspended in 30 ml toluene. Subsequently a mixture of toluene and tetrahydro furfuryloxypropyl triethoxysilane (0.002 moles for f-1 and 0.006 moles for f-2) was added to the stirred suspension. The resulting mixture was sealed and continuously stirred for 72 h at 353 K. The resulting solid phase was isolated by filtration and thoroughly rinsed with toluene to eliminate any remaining unreacted triethoxysilane. Finally, the material was dried overnight at 373 K. The resulting products were denoted as MCF (f-1) and MCF (f-2) and will be referred to as such throughout this manuscript.

The material's porosity was evaluated using N_2-sorption, conducted on an automated Quantachrome Quadrasorb system at 77 K. Before analysis, the samples underwent degassing at 393 K for 16 h. *In situ* diffuse reflectance infrared FT (DRIFT) measurements were performed using a Nicolet 6700 Fourier transform IR (FT-IR) spectrometer. To prepare the samples for analysis, they were diluted in KBr (2 wt%) and heated under vacuum to 393 K. Following a 30-min equilibration time and keeping the temperature constant, 100 scans were performed in the region of 4000–500 cm^{-1} with a resolution of 4 cm^{-1}. Thermogravimetric analyses (TGA) were conducted using a Mettler Toledo TGA/DSC 3+ star system, in cups of 150 μL and 80 mL min^{-1} flow of pure O_2. The TGA results were cross-referenced with the N_2-sorption analysis (BET surface area) to estimate the surface functional group density of the modifier molecule. This methodology was previously validated and documented in the existing literature.[63,64] The analysis of the TGA-profile considered the mass loss between 423 K and 1073 K, assuming that toluene, used as a solvent and rinsing agent in the post-synthesis modification protocol, had evaporated below this temperature.

2.3. Experimental setup and procedure

The schematic layout of the experimental setup employed in this work is presented in Fig. 1. The binary H_2-THF hydrate formation tests were performed in a Swagelok stainless steel cylindrical reactor (316L-50DF4-150; designed pressure: 34.4 MPa) with an effective inner volume of 150 cm^3. The temperature within the reactor was kept cold and stable (measured using a K-type thermocouple, ± 0.1 K; Testo SE & Co. KGaA) by immersing it in a circulating water–ethylene glycol bath (CORIO CP-1000F, JULABO GmbH, stability: ± 0.03 K). The pressure in the reactor was monitored every second using a pressure transmitter acquired from KELLER AG für Druckmesstechnik (PAA3X-30 MPa; range of 0–30 MPa absolute, with ± 0.01% FS accuracy).

All experiments were performed in accordance with the previously reported standard procedure.[45,64,65] In summary, the reactor was thoroughly cleaned with H_2O and dried to remove contaminants/impurities before commencing any experiment.

Table 1 Description of chemicals

Chemical name	Purity	Source
P123 ($EO_{20}PO_{70}EO_{20}$)	Average Mn ~5800	Sigma-Aldrich
Ammonium fluoride (NH_4F)	95%	
1, 3, 5-trimethylbenzene (mesitylene)	99%	
Tetraethylorthosilicate (TEOS)	99%	
Toluene	99%	
Tetrahydro furfuryloxypropyl triethoxysilane	97%	

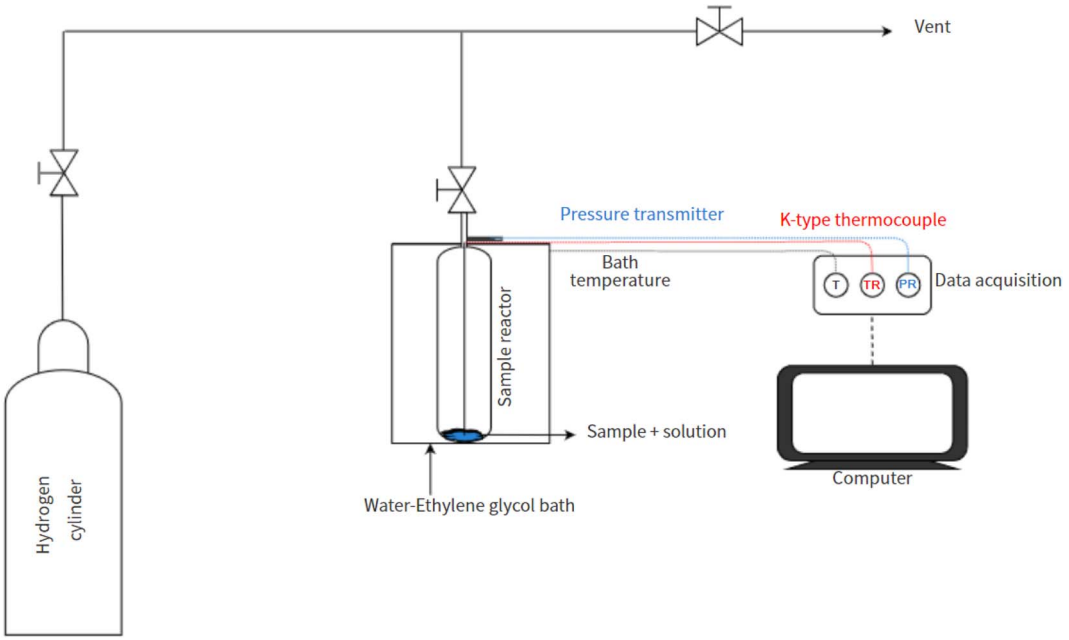

Fig. 1 The schematic of the experimental setup.

To carry out the H_2 uptake experiments, 5.56 mol% THF solution was added to 0.5 g of the synthesized material (dried overnight at 343 K) based on 100% pore volume saturation. To remove any atmospheric gases the reactor was subsequently subjected to at least 10 rapid pressurization (0.2 MPa) and depressurization (0.12 MPa) cycles with H_2 gas. The reactor was then immersed in a water–ethylene glycol bath at 298 K before gradual pressurization with H_2 gas to 7 MPa. Sufficient time was allowed for the system to stabilize under these thermodynamic conditions before cooling the reactor to the experimental temperature. The maximal H_2 storage capacity of the binary H_2-THF clathrate hydrate was considered to have been attained when no considerable pressure reduction ($0.02 \pm 1 \times 10^{-4}$ MPa in 30 min) was observed. Each experiment in this study was performed in triplicate.

The amount of H_2 gas consumed during hydrate formation at any given real-time was quantified using the compressibility factor equation of state as shown in eqn (1):

$$\Delta n_{H_2,t} = \frac{V_r}{RT}\left[\left(\frac{P}{z}\right)_{t=0} - \left(\frac{P}{z}\right)_t\right] \quad (1)$$

with $\Delta n_{H_2,t}$ being the moles of H_2 gas consumed at time t; V_r is the gas-phase volume in the reactor measured using the helium expansion method;[65] R is the ideal gas constant; T and P respectively are the temperature and pressure within the reactor and z is the compressibility of H_2 gas calculated using the Lemmon–Huber–Leachman correlation.[66]

The normalized H_2 gas uptake (NG_t) and the percentage of H_2O to hydrate conversion were quantified using eqn (2) and eqn (3) and 4, respectively.

$$NG_t = \frac{\Delta n_{H_2,t}}{n_{H_2O}} (\text{moles of } H_2/\text{moles of } H_2O) \quad (2)$$

$$\text{WtH}(\%) = \frac{(\Delta n_{H_2,t} + \Delta n_{THF}) \times H_n}{n_{H_2O}} \times 100 \quad (3)$$

$$\Delta n_{THF} = \Delta n_{H_2,t} \times \frac{\text{number of large cages}}{\text{number of small cages}} \quad (4)$$

with n_{H_2O} representing the moles of H_2O introduced into the reactor; Δn_{THF} is the moles of THF consumed for hydrate formation, assuming that THF solely occupies the hexakaidecahedron cages of the expected sII clathrate hydrate, and H_n is the hydration number, which is considered to be 5.67 in order to comply with previously reported binary H_2-THF sII clathrate hydrate studies.[45,67]

The volumetric gas storage capacity was determined using eqn (5),[19]

$$\text{Volumetric } H_2 \text{ storage capacity}\left(\frac{\text{volume of gas at STP}}{\text{volume of hydrate}}\right) = K \times NG_t \quad (5)$$

$$K = \frac{v}{\frac{M_{w,hyd}}{(\rho_{hyd} \times n_{wh})}} \quad (6)$$

$$M_{w,hyd} = (136 \times 18.01) + (8 \times 72.11) + (16 \times 2.016) \quad (7)$$

$$\rho_{hyd} = \frac{M_{w,hyd}}{(A \times \lambda^3)} \quad (8)$$

where the proportionality coefficient K is defined as shown in eqn (6), v is the gas volume under STP conditions (22.4 cm^3 $mmol^{-1}$ of gas), $M_{w,hyd}$ is the molecular weight (g mol^{-1}) of sII clathrate hydrate considering the thermodynamic promoter used in this study (THF) and is calculated as shown in eqn (7),

n_{wh} is the mole of H_2O per mole of sII clathrate hydrate (*i.e.* 136), and ρ_{hyd} (g cm^{-3}) is the hydrate density, calculated using eqn (8), with A the Avogadro constant (6.023×10^{23} mol^{-1})[68] and λ the sII hydrate lattice parameter which is 17.145 Å when THF is used as a promoter and pressurized with H_2 gas in the bulk.[69]

The rate of H_2 hydrate formation was determined by applying a discrete first-order forward difference approach, as shown in eqn (9), where Δt (1 min) is the time difference between two observations.

$$\frac{dN_t}{dt} = \left(\frac{d\Delta n_{H_2}}{dt}\right) \approx \frac{\Delta n_{H_2,t+\Delta t} - \Delta n_{H_2,t}}{\Delta t} \quad (9)$$

2.4. Characterization of the confined clathrate hydrate phase

The crystal structure of the clathrate hydrate phase formed in an MCF (f-1) host material mixed with an amount of 5.56 mol% THF solution corresponding to 100% of its pore volume, and subsequently pressurized to 7 MPa with H_2 gas and cooled to 265 K, was established by transmission X-ray diffraction using a B STOE STADI P combi diffractometer with a focusing Ge(111) monochromator (CuKα_1 radiation, λ = 0.154 nm) in a high throughput set-up in transmission geometry. Samples were collected from the reactor, ground in a mortar filled with liquid nitrogen (LN_2) and finally transferred to a sample holder which had been submerged in LN_2 up until the transfer. The metal sample holder was retrofitted with a Kapton® bottom film to withstand the low LN_2 temperature (77 K) required for the stability of the clathrate hydrate phase at atmospheric pressure. PXRD data were recorded using a 140° curved image plate position sensitive detector (IP PSD) from −17.5 to 62.5° 2θ. To account for reflections originating from the MCF host material, a diffraction pattern of the dry MCF (f-1) material was recorded as a reference. X-ray diffraction experiments at liquid nitrogen (LN_2) temperature (77 K) and atmospheric pressure were performed in a metal sample holder with a Kapton® bottom film. The low temperature ensured the stability of the clathrate hydrate phase under these conditions. Before XRD analysis, the H_2-THF clathrate hydrate samples were first ground in a mortar filled with LN_2 and then transferred to the metal sample holder which had been submerged in LN_2 up until the transfer.

Incorporation of H_2 in 5^{12} cages of the sII clathrate hydrate lattice was observed using *in situ* high-pressure ^{1}H nuclear magnetic resonance (NMR) spectroscopy at 800 MHz. ^{1}H NMR spectra were acquired using a static 5 mm BBO probe head operating at a Larmor frequency of 801.25 MHz and a Bruker Avance Neo console. The temperature was regulated using a BCU II unit. In order to minimize the ^{1}H background signal of the host material and facilitate identification of all components in spectra, the MCF (f-1) material was rinsed 3 times with D_2O and subsequently dried at 363 K under vacuum. Approximately 30 mg of dried D-exchanged MCF (f-1) sample was packed in a 5 mm high-pressure NMR cell built according to the design by Houlleberghs *et al.*[70] before adding 60 μL of a 5.56 mol% THF-D_2O mixture to the system. The tube was pressurized to 7 MPa with H_2 gas before transferring to a pre-cooled (265 K) NMR probe head and allowing the system to equilibrate for 10 h. Following shimming, 48 transients were recorded for each ^{1}H NMR spectrum using a 30° pulse with 18 kHz RF strength and a repetition delay of 10 s. Chemical shift referencing was carried out with respect to TMS, using ethylbenzene (10% in chloroform-d) as a secondary reference with δ (^{1}H) = 1.22 ppm. Spectral decomposition was performed using dmFit software using Gaussian lineshapes.[71]

3. H_2-THF binary hydrate kinetics

The kinetic regime of post-induction time H_2 gas uptake was analyzed using the widely adopted Johnson–Mehl–Avrami–Kolmogorow (JMAK) model,[72–80] as shown in eqn (10). This model was established to describe the kinetics of phase change under isothermal/isotropic conditions with a linear growth rate and random nucleation.

$$\alpha_{WtH} = 1 - \exp(-k(t)^n) \quad (10)$$

where α_{WtH} is water-to-hydrate conversion at time t, k is the crystallization rate constant and n is the Avrami exponent.

However, in a later phase of hydrate growth, the kinetics of hydrate crystallization is often impeded due to the poor diffusion of guest gas (H_2) or H_2O through the hydrate layer.[81,82] Considering this, the kinetics of the experimental data were also analyzed by adopting Hay's two-stage crystallization kinetic model,[83] as given in eqn (11), which can represent both the initial hydrate growth based on the JMAK model (first term in eqn (11)) and the hydrate growth owing to diffusion (second term in eqn (11)),

$$\alpha_{WtH} = \alpha_P(1 - \exp(-k_P t^n))(1 + (k_s t^{0.5})) \quad (11)$$

where α_{WtH} is the water-to-hydrate conversion at time t and α_P is the water-to-hydrate conversion at the end of the reaction-controlled primary crystallization process. k_P and k_s are the rate constants for reaction-controlled primary and diffusion-controlled secondary crystallization growth, respectively. n is the Avrami exponent. Additional details about the analysis are provided in the Results and discussion section.

The efficacy of the kinetic models in predicting water-to-hydrate conversion is evaluated using average absolute deviation (AAD) as shown in eqn (12),

$$AAD = \frac{1}{N}\sum_{i=1}^{N}|E_i^{\alpha} - P_i^{\alpha}| \quad (12)$$

N is the number of datasets and E_i^{α} and P_i^{α} are experimental and predicted water-to-hydrate conversion respectively.

4. Results and discussion

4.1. Host material characterization

N_2-sorption (Fig. 2a) proved the successful formation of the MCF (n-f) material. The presence of the swelling agent pushed for the formation of considerably larger pores as compared to

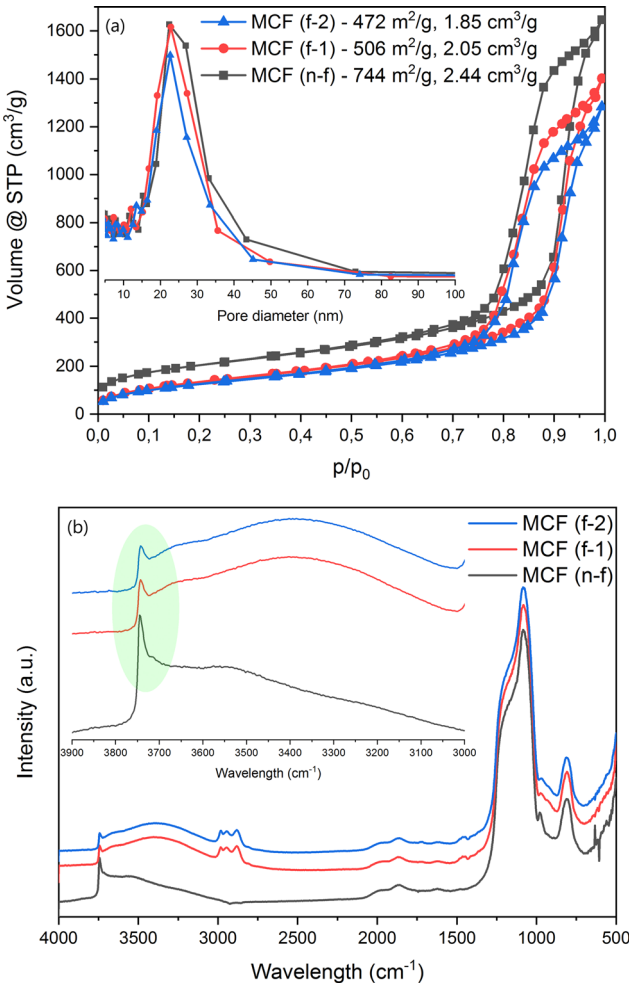

Fig. 2 (a: top) N_2 sorption and (b: bottom) *in situ* DRIFT analyses of the materials.

a standard SBA-15 material.[84] The maximum size of the ultra-big mesopores determined by the BJH method is approx. 22 nm, while the BET surface area and total pore volume reach 744 m^2 g^{-1} and 2.44 cm^3 g^{-1}, respectively. Following the procedure of post-synthesis modification, a decrease in both surface area and total pore volume is observed (Fig. 2a), serving as an initial confirmation of the successful grafting process. The most important band observed during the *in situ* DRIFT spectral analysis refers to the presence of silanol groups on the surface, localized at around 3745 cm^{-1} (Fig. 2b). The decreased intensity of this band after the grafting procedure suggests the chemical attachment of the modifier molecule. In other words, fewer Si–OH groups are present on the surface of the material after the modification procedure takes place, which directly implies that these groups are involved in the surface reactions. Next, the features belonging to the silica material are present in all the samples, while the bands at around 2981, 2944, 2881 and 1456 cm^{-1} are related to the CH_x groups of the modifier.[62,85]

Thermogravimetric analysis (Fig. S1†) showed a consistent mass loss above 423 K for the modified MCF materials (12–13%). It is clear that increasing the amount of the modifier did not achieve a considerably higher modification degree. This might be connected to the surface becoming saturated with the modifier molecule, leading to steric interactions that restrict the chemical grafting process. The carbon content exhibits variation between the two modified samples, resulting in an approximately 7% increase in the density of the groups on the surface of MCF (f-2), totaling 0.75 g nm^{-2} compared to MCF (f-1). To conclude here, all the results presented above suggest a successful modification of the MCF material with the THF-ending molecule.

4.2. Characterization of the clathrate hydrate phase

The identity of clathrate hydrate was confirmed to be sII clathrate hydrate using XRD analysis of the product obtained with MCF (f-1) as a porous host. Next to the sII clathrate hydrate also hexagonal ice was found (Fig. S2†). At present it cannot be distinguished if the impurity was formed in the reactor or by condensation and subsequent freezing of moisture from the air during the XRD analysis.

Enclathration of H_2 in 5^{12} cages of the sII hydrate structure was demonstrated using *in situ* high-pressure ^1H NMR spectroscopy (Fig. 3). Subtracting the ^1H NMR spectrum of pure THF sII clathrate hydrate confined in MCF (f-1) (Fig. 3a) from the spectrum of the binary H_2-THF clathrate hydrate formed at the same temperature in the presence of 7 MPa of H_2 pressure (Fig. 3c) yielded a difference spectrum containing the resonance of gaseous H_2 and H_2 occupying the small cage of the clathrate hydrate (Fig. 3c, inset). To identify the signature of gaseous H_2 and enable assignment, the ^1H NMR spectrum of a dry MCF (f-1) material pressurized with 7 MPa H_2 gas was measured (Fig. 3b). Decomposition of this spectrum revealed two resonances at 5.1 and 5.2 ppm respectively, which are associated with gaseous H_2 in the presence of the host material. Decomposition of the difference spectrum between confined binary H_2-THF clathrate hydrate and confined pure sII THF clathrate hydrate revealed the presence of 3 spectral components (Fig. 3c, inset), two of which (A and B) were also present in the spectrum of the dry host material pressurized with H_2 gas. The third resonance (C) at 4.2 ppm can therefore unequivocally be assigned to H_2 molecules residing in the 5^{12} cages of the sII hydrate structure. A similar resonance was reported by Lee *et al.*[21] in their pioneering work on binary sII H_2-THF clathrate hydrate.

4.3. Effect of functionalized porous materials on H_2 storage

The storage capacities of H_2 in the binary H_2-THF clathrate hydrate were investigated using an unstirred reactor filled with ≈0.5 g of porous material and 5.56 mole% of aqueous THF solution. All the experiments were conducted at 265 K with an initial H_2 gas pressure of 7 MPa and all systems were saturated with a stoichiometric solution (5.56 mol%), corresponding to 100% of pore volume saturation of each material. The host material consisting of hydrophilic silica-based materials (MCF) and the same material grafted with THF-like functional groups (hydrophobic) were used in the experiments to evaluate the impact of the grafting on hydrate formation rates and H_2 storage capacities. The primary distinctions between materials

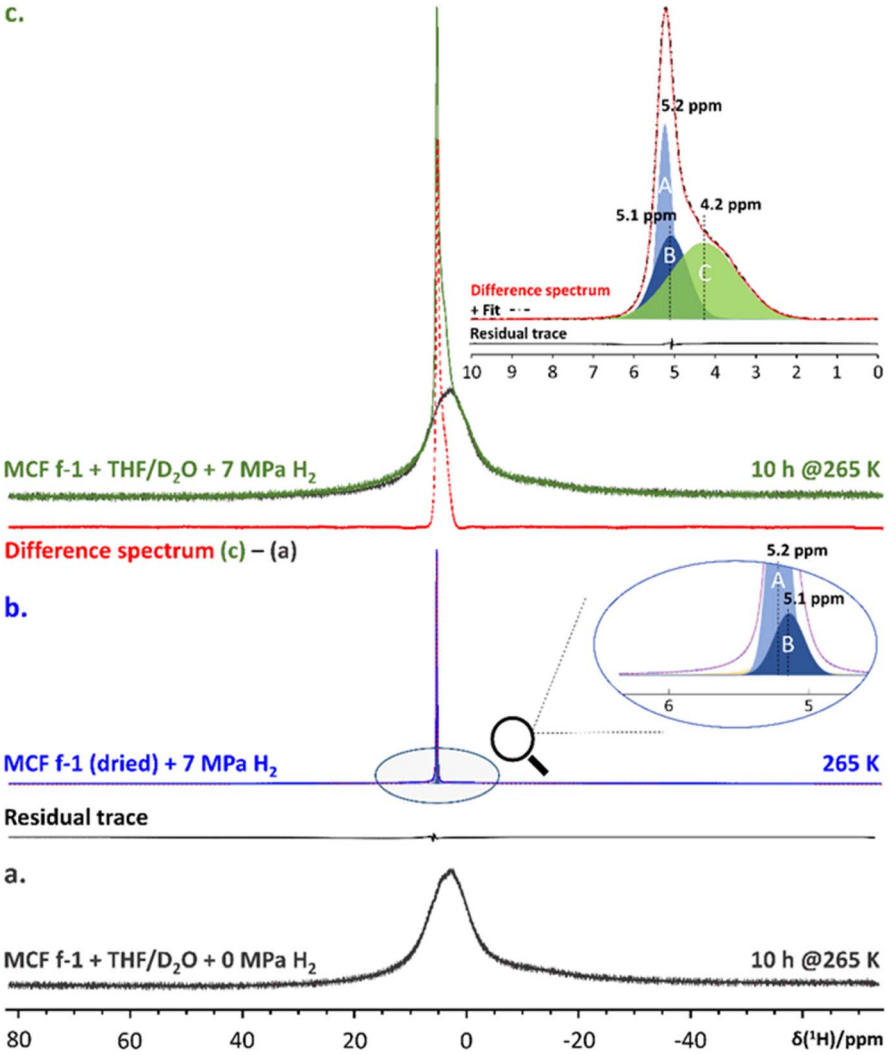

Fig. 3 (a). ^{1}H NMR spectrum of MCF (f-1) + 5.56 mole% THF/D_2O + 0 MPa H_2 measured after equilibration for 10 hours at 265 K (black trace). (b). ^{1}H NMR spectrum of D_2O-exchanged and subsequently dried MCF (f-1) pressurized with 7 MPa H_2 recorded at 265 K (blue trace). (Inset): zoom-in highlighting the most relevant spectral components, *i.e.*, 'A' and 'B', and their corresponding chemical shifts. The added residual trace reflects the accuracy of the modelled fit (dotted red trace). (c). ^{1}H NMR spectrum of MCF (f-1) + 5.56 mole% THF/D_2O + 7 MPa H_2 after 10 hours at 265 K (green trace). The red trace below shows the ^{1}H NMR spectrum obtained from computing the difference between spectra (c) and (a). (Inset): spectral decomposition of the resulting difference spectrum. The different components, *i.e.*, A, B and C, are color coded in accordance with previous decompositions. The residual trace reflects the accuracy of the modelled fit (dashed/dotted black trace).

are their pore volumes and the number of carbons per nm^2 as a result of functionalization. Table 2 summarizes the list of experimental conditions, H_2 storage capacities and other analyzed outcomes from this work. Note that porous media can influence the phase equilibrium of hydrate formation and thus can serve as thermodynamic inhibitors, shifting the phase boundaries to significantly higher pressures and lower temperatures compared to bulk systems. Such effects are expected to become increasingly important as the pore size decreases and the hydrophilicity increases.[49,86,87] To assess the occurrence of such effects in our study, a comparative phase equilibrium analysis of binary H_2-THF clathrate hydrates in the MCF (f-1) material and in the bulk system was performed. As can be seen from Fig. S3,† the presence of a porous host indeed induces a small shift in the phase diagram (up to 4 K at the lowest experimental temperature), but overall its effect is limited given the large mesopore size of 25 nm and the more hydrophobic nature of the grafted tetrahydro furfuryloxypropyl triethoxysilane functional groups. This small thermodynamic penalty does however not outweigh the observed kinetic promotion, where dispersion of the aqueous phase throughout the modified porous matrix coupled with favourable pore wall–water interactions enables larger amounts of clathrate hydrate to be formed under non-stirred conditions in hours rather than days as compared to non-confined, bulk systems under similar experimental conditions.

Fig. 4 shows the amount of H_2 enclathrated during binary H_2-THF hydrate formation in MCF (f-1 and f-2) hydrophobic and MCF (n-f) hydrophilic silica based porous materials. Time zero in this figure corresponds to the commencement of

Table 2 Summary of experimental observation for H_2/THF(5.56 mol%)/H_2O hydrate in THF-like functionalized and non-functionalized silica based porous materials under different thermodynamic conditions[a]

Porous system	P (MPa)	T (K)	NG_t (mmoles of H_2 per mole of H_2O)	WtH (%)	$q_{H_2}^{w}$ (wt%)	$q_{H_2}^{A}$ (wt%)	$q_{H_2}^{T}$ (wt%)	Volumetric H_2 storage (v/v)
MCF(n-f)	7	265	13.53	11.50	0.15	0.30	0.10	13.58
MCF(f-2)	7	265	16.15	13.73	0.18	0.27	0.11	16.21
MCF(f-1)	7	265	18	15.31	0.21	0.34	0.13	18.06
MCF(f-1)	7	268	14.06	11.96	0.16	0.27	0.1	14.12
MCF(f-1)	7	262	46.77	39.78	0.52	0.88	0.33	46.95

[a] $q^{w}_{H2}(wt\%) = \frac{m_{H_2}}{(m_{H_2O} + m_{H_2})} \times 100$, $q^{A}_{H_2}(wt\%) = \frac{m_{H_2}}{(m_{solid} + m_{H_2})} \times 100$, $q^{T}_{H_2}(wt\%) = \frac{m_{H_2}}{m_{tot}} \times 100$, m_{H_2} = mass of H_2, m_{H_2O} = mass of H_2O, m_{solid} = mass of solid, and m_{total} = mass of H_2O + mass of solid + mass of H_2.

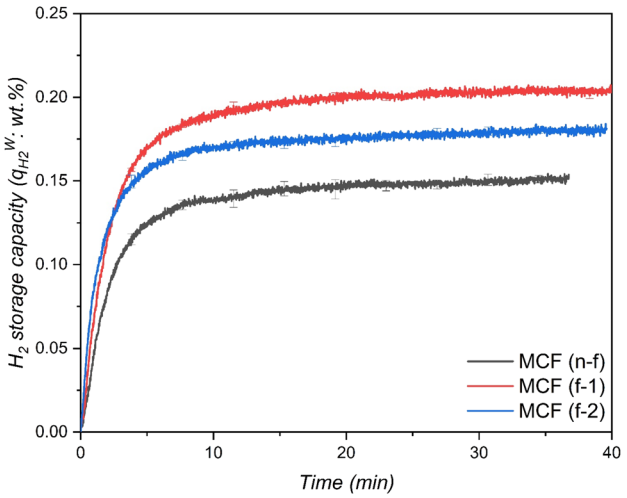

Fig. 4 H_2 storage capacity in THF-like functionalized MCF (f-1 and f-2) hydrophobic and non-functionalized MCF (n-f) hydrophilic porous materials at 265 K with an initial pressure of 7 MPa.

hydrate formation observed from the first temperature spike due to the exothermic nature of the process and all three gas uptake curves also demonstrate the consistency of hydrate formation with a minor standard deviation. As shown in Fig. 4, all three materials exhibit rapid hydrate formation before tapering off to a steady state, and the characteristic time t_{90}, defined as the time required for the system to reach 90% of the maximum obtained gas uptake, was less than 7.5 min for all the systems, implying that this parameter could be a critical criterion in evaluating the kinetic performance of gas uptake as well as hydrate formation. It can also be seen from the figure that the THF-like functionalized materials MCF (f-1 and f-2) showed an excellent promoting effect on H_2 storage compared to non-functionalized material MCF (n-f) despite having a pore volume ~16% and 24% lower than MCF (n-f), respectively. For instance, MCF (f-1), at 265 K, attained a maximum H_2 storage capacity ($q_{H_2}^{w}$) of 0.21 wt%, which corresponds to ~15.31% of water-to-hydrate conversion and 18 mmol H_2 per mol H_2O, while MCF (n-f) attained only 0.15 wt% and ~11.50% of water-to-hydrate conversion which is 28.6% and 24.8% less than MCF (f-1), respectively. It is also evident from the gas uptake curves that there also exists an optimal amount of tuning THF-like moieties for enhancing the H_2 storage, where lowering the number of carbons per nm^2 showed a better gas uptake compared to MCF (f-2) having ~7% higher carbons per nm^2 (which is relatively more hydrophobic than MCF (f-1)) and MCF (n-f) which is a completely hydrophilic material. It is also important to mention that in order to corroborate the suggestions from Lee *et al.*,[21] THF-like functionalized and non-functionalized materials were also tested with 0.1 and 0.3 mol% THF solution; however, no clathrate formation was observed at 265 K for a period of 6 h. The induced hydrophobicity generated by the organic molecules grafted on the surface of the MCF directly affects the interaction of the material with water. In this regard, as already proved before, the organic groups are not allowing the water to interact very strongly with the surface of the SiO_2 material and provide a favorable environment for stabilizing clathrate cages and promoting the encapsulation of hydrogen molecules within those cages.[54,57] On top of this, one can assume that the enhanced mobility induced by the ether (containing 5 atoms) linker may allow the THF-ending group to have an influence on the water structure disruption, lowering nucleation barrier.[88]

4.4. Effect of temperature on H_2 storage

The material that demonstrated higher H_2 uptake at 265 K was further investigated at two different temperatures to determine its H_2 storage capacities. Typically, lower temperatures for hydrate formation demonstrate higher driving force at constant pressure indicating improved gas enclathration. However, few studies[89,90] reported that the gas storage capacities increased with an increase in temperature, implying that lowering the driving force enhances gas storage capacity. In this perspective, two different temperatures, one lower than 265 K and one higher than 265 K were chosen to investigate the effect of the hydrate formation rate and H_2 enclathration. The corresponding experiments were performed at 262 K and 268 K with an initial H_2 gas pressure of 7 MPa and both the systems were saturated with 5.56 mol% of THF solution, which corresponded to 100% of pore-volume saturation. Fig. 5 exhibits H_2 storage capacity of the systems at 268 K, 265 K and 262 K. As can be seen, the temperature has a significant impact on the hydrate formation rate and H_2 storage capacities, where a decrease in temperature from 268 K to 262 K resulted in a substantial

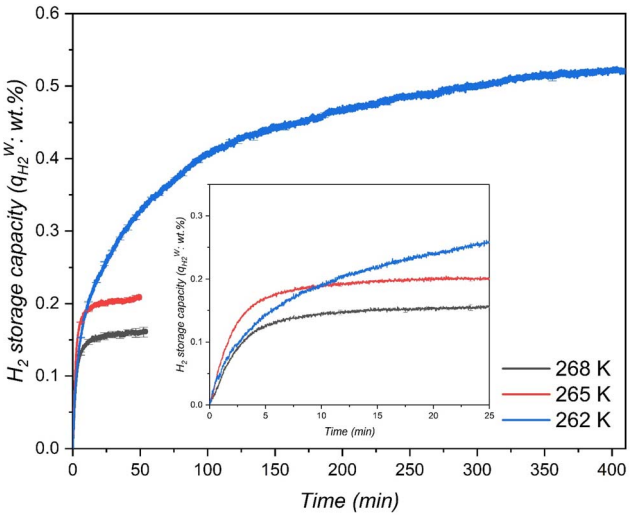

Fig. 5 H_2 storage capacity in the THF-like functionalized MCF (f-1) porous material at three different temperatures with an initial pressure of 7 MPa.

increase in H_2 enclathration, attaining a maximum storage capacity of ~0.52 wt% at the lowest temperature. These findings are consistent with Tian and Zhang simulation work,[91] which indicated that the maximal H_2 storage capacity in a binary H_2-THF hydrate can be obtained at 260 K at constant pressure. Similarly, results from Liu *et al.*[92] also support our findings by demonstrating that THF hydrate formation diminishes with increasing temperature, which consequently affects H_2 enclathration in the small cages (5^{12}).

Meanwhile, the material MCF (f-1) also showed higher H_2 storage capacity than H_2/THF hydrate systems and relatively similar storage capacities compared to H_2/1,3-dioxolane systems using stirring reactors (Table 3). Nevertheless, it is worth mentioning that the pressures used in these stirring systems are at least 75% higher than the pressures used in this work. This indicates that the surface grafted THF-like functionalized porous materials show better mass transfer performance for a static/unstirred H_2 storage system compared to stirring systems (which are energy intensive). Nevertheless, at the end of hydrate growth reaching a steady state the total H_2 storage capacity at 262 K was 2.47 and 3.25 times higher than that in the case of 265 K and 268 K respectively, which corresponds to 39.78% water-to-hydrate conversion and 46.77 mmol H_2 per mol H_2O. Fig. 6 also displays rapid hydrate growth in the first 2 min at all the temperatures, where the initial rate of hydrate formation increased with decreasing temperature from

Table 3 H_2 storage capacity in sII hydrates below 15 MPa using promoters (stoichiometric conc.)

System	P (MPa)	T (K)	H_2 storage capacity (wt%)	Occupancy of 5^{12} cages[a] (%)	Ref.
This work	7	268	0.16	6.08	—
	7	265	0.21	7.97	
	7	262	0.52	19.84	
Powdered THF hydrate	6.7	270	0.36	13.63	27
	12.2		0.46	17.70	
	6.2		0.38	14.56	
	12.1		0.55	21.13	
	12.4		0.32	12.28	
Powdered THF hydrates	10.7	277.15	0.19	7.23	38
	11.4		0.26	9.90	
Powdered THF hydrates	6.5	269.5	0.23	8.75	99
	6.5	269.5	0.23	8.75	
	6.5	269.5	0.20	7.61	
	8.4	269.5	0.25	9.52	
	6.5	269.5	0.23	8.75	
	3.6	269.5	0.19	7.23	
	6.5	266.7	0.26	9.90	
	6.5	269.5	0.23	8.75	
	6.5	275.1	0.21	7.99	
THF-bulk solution/stirring	7.0	278.2	0.14	5.25	67
	5.0	278.2	0.12	4.40	
	5.0	278.2	0.13	4.76	
	5.0	278.2	0.10	3.92	
Powdered THF hydrate	5.0	265.1	0.18	6.85	100
	5.0	269	0.16	6.10	
	5.0	273.2	0.15	5.71	
Powdered DXN hydrate	12.0	233	0.4	15.25	101
THF-bulk solution/stirring	13	279.2	0.183	6.96	102
DIOX-bulk solution/stirring	12.3	271.15	0.216	8.22	20
THF in porous media	11.6	270	0.4	15.25	41
ECP-bulk solution	12.2	273.25	0.310	11.81	37

[a] Estimated based on two H_2 molecules in a single small cage.

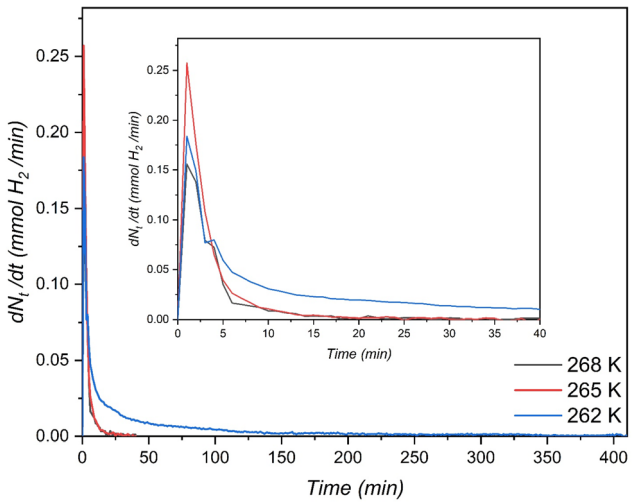

Fig. 6 Rate of H_2-THF binary hydrate formation in the THF-like functionalized (f-1) porous material at three different temperatures with an initial pressure of 7 MPa.

268 K to 265 K and then dropped down quickly to near-zero after 30 min. However, lowering the temperature to 262 K showed a slight decrease in the initial rate of hydrate formation (which is evident from Fig. 5 (inset)) compared to 265 K, followed by a very gradual reduction, and reaching near-zero at about 350 min, indicating diffusion-controlled hydrate growth. Further explanation of hydrate growth kinetics is presented in the next section.

It could be intriguing to compare the findings of various research groups endeavoring to enhance H_2 storage in clathrate hydrates. Nevertheless, a direct comparison of the absolute values pertaining to the hydrate growth rate, maximum gas stored capacity, and other parameters obtained from different research laboratories might not be a reliable way to ascertain which one leapfrogged the other as the experimental procedures, reactor setups, and methodologies employed by different groups could significantly influence the results, which could also be a major contributing factor to the observed differences in kinetics of hydrate formation, possibly involving mass transfer limitations. However, it is exemplary to make a comparison between the studies focusing on H_2 storage capacity in the binary H_2-THF clathrate hydrate, which is presented in Table 3.

Scientifically, it is well-established that under extremely high pressures, H_2 can form sII hydrate, reaching 5.6 wt%, with both small (5^{12}) and large cages ($5^{12}6^4$) accommodating two and five H_2 molecules, respectively.[15,93] However, when THF (a thermodynamic promoter) is introduced in stoichiometric concentrations, the H_2 molecules can only occupy small cages, while large cages are left for THF. Consequently, the overall storage capacity decreases to 1.3 wt% and 2.5 wt% when one and two H_2 molecules occupy a small cage, respectively. From the data presented in Table 3, it is evident that in a H_2-promoter (stoichiometric conc.) H_2O system under various thermodynamic conditions, the maximum H_2 storage capacity falls below 1.3 wt%. This indicates that either the fractional H_2 occupancy in the small cages is less than 1 or not all small (5^{12}) cages are filled under those specific conditions. However, this limitation can be overcome by increasing the pressure of the system, which leads to an enhancement in H_2 storage capacity. Furthermore, Table 3 demonstrates that by employing solid-state tuning of the material, it is possible to improve the H_2 storage capacity significantly even at relatively low pressures when compared to values reported in the literature. While powder-THF hydrate exhibits better H_2 enclathration, it is essential to note that the fine THF hydrate particles revert to a liquid phase upon melting. This characteristic makes them unsuitable for continuous cycles of H_2 storage and release, thereby limiting their practical applicability in certain situations.

4.5. Kinetic analysis

In this study, the formation kinetics of hydrates at different temperatures were investigated using two distinct kinetic models, as mentioned earlier. The predicted kinetic curves of hydrate formation from the JMAK model[73] (eqn (10)) are depicted in Fig. S4,† and the corresponding values of the rate constant (k) and the Avrami kinetic exponent (n) were determined and are presented in Table S1.† The Avrami kinetic exponent (n) is commonly used to interpret the growth geometry and the degree of crystallization during hydrate formation in a porous medium.[94] The value of the Avrami exponent (n) can provide insights into the growth dimension of hydrate crystals. A value of $n = 3$ indicates instantaneous three-dimensional growth from a spherical nucleus, $n = 2$ suggests instantaneous two-dimensional growth, and $n = 1$ signifies one-dimensional growth. However, interestingly, the regressed exponent values (n) obtained for the entire growth period, as shown in Table S1,† are consistently less than 1 for all conditions. This indicates that the hydrate crystals experienced instantaneous one-dimensional growth, followed by a decrease in hydrate nucleation and growth rates. This decrease in growth rates could be attributed to the presence of mass transfer resistance in the system. Similar low Avrami exponent values for hydrate growth were also reported by other researchers.[77,95,96] Conclusively, the predictive power of the JMAK model revealed limitations in evaluating the hydrate growth at both the beginning or later stages of the growth kinetics.

The limitations of single-step kinetic models have led to a preference for using an integrated multistep model, which offers a more accurate representation of hydrate kinetics. To achieve this, the model proposed by Hay[83] has been adopted and adapted for evaluating the hydrate growth kinetics at both the reaction-controlled stage (primary growth) and the diffusion-controlled stage (secondary growth). Hay's model, in a more detailed version, was previously described in their earlier work on crystallization kinetics.[97,98] This integrated approach allows for a more comprehensive understanding of the hydrate formation process by considering the distinct contributions of both primary and secondary growth stages. By incorporating these stages into the model, a more accurate depiction of the overall hydrate kinetics can be obtained,

improving our insights into the complex nature of hydrate formation. As indicated in eqn (11), the total water-to-hydrate conversion (α_{WtH}) can be categorized into two components: the water-to-hydrate conversion in the primary growth stage and the secondary growth stage, as shown in eqn (13).

$$\alpha_{WtH} = \alpha_{WtH,P} + \alpha_{WtH,S} \quad (13)$$

Here, $\alpha_{WtH,P}$, the primary crystal growth stage, attributed to the rapid nucleation and hydrate growth was analyzed using the JMAK model (eqn (14)), assuming that the primary growth stage ends before the onset of the diffusion-controlled regime *i.e.*, the secondary growth stage (α_P).

$$\alpha_{WtH} = \alpha_P(1 - \exp(-k_p t^n)) \quad (14)$$

where k_p is rate constant for primary crystallization growth and n is the Avrami exponent. Eqn (14) can also be rewritten by applying a double logarithm as shown in eqn (15).

$$\ln(-\ln(1-\alpha_{WtH,P}/\alpha_P)) = n\ln(t) + \ln(k_p) \quad (15)$$

In this analysis, exponent n was set to 1 assuming one-dimensional growth and the value of the adjustable parameter, α_P, was chosen from the best linear fit to eqn (15) based on the coefficient of determination (R^2) (for MCF (f-1) at 265 K: Fig. S5†). Finally, the corresponding value of $\ln(k_p)$ was obtained from the intercept. The water-to-hydrate conversion in the secondary hydrate growth stage is defined as shown in eqn (16).

$$\alpha_{WtH,S} = \alpha_{WtH,P}(k_s t^{0.5}) \quad (16)$$

By substituting eqn (16) and eqn (14) into (eqn (13)), the complete kinetic model for the process is derived, as described in (eqn (11)). The kinetic rate constant governing the secondary growth or crystallization stage was determined by plotting $\left[\left(\frac{\alpha_{WtH} - \alpha_P}{\alpha_P}\right)\right]$ against $t^{0.5}$ and calculating the slope of the resulting linear fit. These rate constants and α_P, obtained from this study, are summarized in Table 4 and the predicted kinetic curves of hydrate formation from the Hay model are depicted in Fig. 7.

Table 4 reveals that the secondary kinetic rate constant (k_s) decreases to a lower value after the initial growth stage, regardless of the driving force applied. This reduction can be attributed to slower conversion rates due to mass transfer resistance within these porous media, particularly upon reaching a certain water-to-hydrate conversion level.

Table 4 Regressed values of rate constants (k_p and k_s), from the Hay[83] model

		Multistep kinetic model		
System	T (K)	k_p (min^{-1})	k_s (min^{-1})	AAD
MCF (f-1)	268	0.38	0.012	0.16
	265	0.48	0.015	0.18
	262	0.17	0.022	0.23

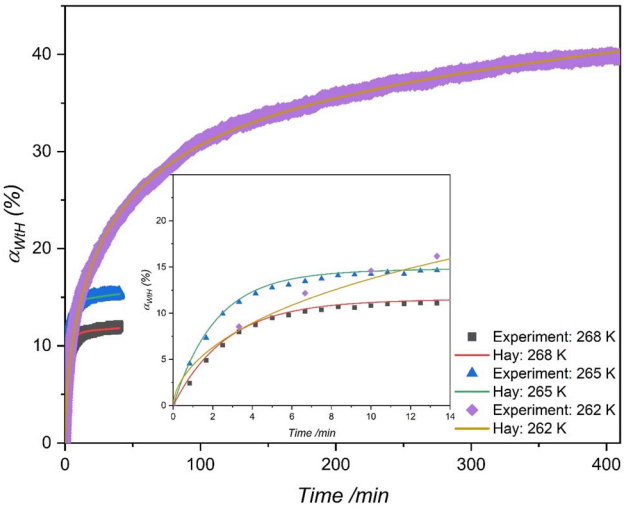

Fig. 7 Comparing the multistep kinetic model (Hay)[83] to experimental data for water-to-hydrate conversion (%) in the THF-like functionalized (f-1) porous material at three different temperatures with an initial pressure of 7 MPa.

Furthermore, the multistage kinetic model consistently demonstrated superior predictive capabilities for hydrate kinetics compared to the JMAK model, as evident from the AAD values. Moreover, the multistage model allows for an insightful examination of the contributions of primary and secondary-stage hydrate growth to the overall water-to-hydrate conversion. For instance, at 262 K, as shown in Fig. S6(c)†, the secondary stage contributes to around 30% of the overall water-to-hydrate conversion. This suggests that the growth of hydrates, equally driven by primary and diffusion-controlled stages, significantly influenced the slow rate of hydrate formation from inception, leading to relatively low-rate constants at very low temperatures. These findings highlight the significance of the multistage kinetic model in understanding hydrate formation dynamics.

4.6. Clathrate hydrate formation pathway

The kinetic model conclusively indicates that the formation pathway for H_2-THF hydrate in porous media involves the concurrent occurrence of primary hydrate growth and diffusion-controlled secondary growth. Unlike sequential pathways where a separate THF hydrate forms first followed by H_2 enclathration, primary growth here involves the direct formation of H_2-THF hydrate (as can be seen from Fig. 8, where a single sharp exothermic peak representing hydrate nucleation coincides with a significant pressure drop, signifying simultaneous hydrate formation and H_2 enclathration occurring at the same time). This initial stage is characterized by rapid hydrate growth within the pore space, where the growing hydrate crystal makes it progressively more challenging for H_2 molecules to reach the growing crystal front creating a diffusion limitation. Despite the diffusion limitations, the inherent high diffusivity of H_2 within clathrate hydrates allows for continued crystal growth until steric hindrance (impingement) occurs. This initial burst of

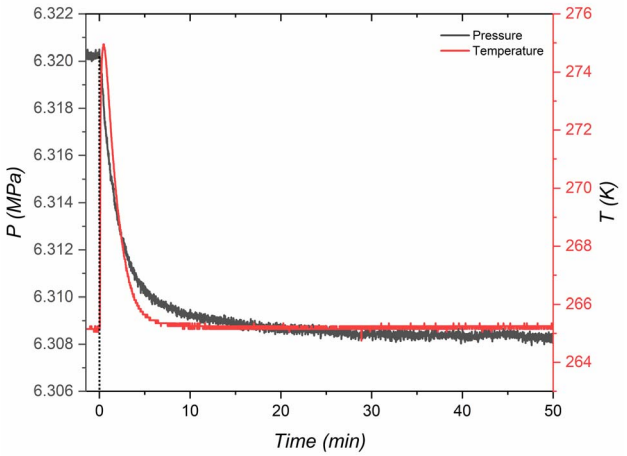

Fig. 8 A single sharp exothermic peak representing hydrate nucleation coinciding with a significant pressure drop inferring simultaneous THF hydrate formation and H_2 enclathration for MCF (f-1) at 265 K.

growth (as observed from relatively high k_P) corresponds to primary crystallization, while the interplay between continued growth and the increasing influence of diffusion limitations ($k_s < k_P$) reflects the concept of secondary growth.

5. Conclusion

This study introduces a new strategy to expedite H_2 storage *via* clathrate hydrates by solid-state tuning of silica-based porous materials (MCF) by grafting promoter-like molecules (THF), leading to a notable enhancement in H_2 enclathration kinetics and storage capacities within a binary H_2-THF hydrate, as compared to conventional bulk stirring systems. The performance of the materials was evaluated under the conditions of 100% pore volume saturation with a stoichiometric concentration of THF solution (5.56 mol%), at 7 MPa in a range of different temperatures (262 K, 265 K, and 268 K) using a volumetric approach. The findings revealed that the modified MFC materials (MCF (f-1) and (f-2)) can enhance the overall H_2 storage capacity compared to the non-modified material (MCF (n-f)). This enhancement could potentially be attributed to the induced hydrophobicity achieved by grafting organic molecules onto the surface of MCF (n-f), which directly influenced the interaction of the material with H_2O, creating a conducive milieu for stabilizing clathrate cages and promoting the encapsulation of H_2 within these cages. Additionally, the mobility engendered by the ether linker is hypothesized to enable the THF-ending group to function as a promoter, perturbing the water structure and lowering the nucleation barrier. MCF (f-1) and MCF (f-2) achieved a maximum H_2 gas uptake of 0.21 wt% and 0.18 wt%, respectively, as opposed to MCF (n-f) which reached 0.15 wt% at 265 K. It is also evident from the gas uptake curves that there also exists an optimal amount of tuning the material that enhances the H_2 storage, where a lower number of carbons per nm^2 showed a better gas uptake. Furthermore, the results also show that the H_2 storage capacity increases with an increase in driving force (*i.e.*, a decrease in temperature), where a maximum storage capacity of 0.52 wt% corresponding to 46.77 mmoles of H_2 per mole of H_2O and 39.78 water-to-hydrate conversions was achieved at 262 K in MCF (f-1). An intriguing aspect of these results is the substantial H_2 storage capacity observed without necessitating supplementary energy-intensive procedures such as agitation or crystal grinding. This underscores the potential of solid-state tuning of porous materials as promoters for H_2 storage within artificially synthesized hydrates. Additionally, this work also employed two distinct models for kinetic analysis of hydrate formation and growth in MCF (f-1) at all driving forces. Notably, the multistage kinetic model exhibited better predictive capabilities for the experimental data (water-to-hydrate conversion), with a commendably low average absolute deviation (AAD). Conclusively, it is also recommended to conduct a comprehensive molecular-level investigation to glean a more profound comprehension of the solid-state tuning effects on the supporting materials in enhancing H_2 storage capacities. Additionally, these insights can contribute to the refinement and upscaling of clathrate-based H_2 storage processes, thereby paving the way for further technological advancements.

Conflicts of interest

The authors declare no competing financial interest.

Acknowledgements

This work received funding from the European Research Council (ERC) under grant agreement no. 834134 (WATUSO). The authors acknowledge VLAIO for Moonshot funding (ARCLATH, no. HBC.2019.0110, ARCLATH2, no. HBC.2021.0254). NMRCoRe is supported by the Flemish Government as an international research infrastructure (I001321N) and acknowledges infrastructure support by Department EWI *via* the Hermes Fund (AH.2016.134) and by the Hercules Foundation (AKUL/13/21). M. H. acknowledges FWO Vlaanderen for an FWO-SB fellowship.

References

1 UNFCC, *Action Taken by the Conference of the Parties Serving as the Meeting of the Parties to the Kyoto Protocol at its Seventeenth Session*, Egypt, 2023, **https://newsroom.unfccc.int/sites/default/files/resource/cmp2022_09_add1_adv.pdf**.
2 E. Tzimas, *et al.*, *Hydrogen Storage: State-Of-The-Art and Future Perspective*, Netherlands, 2003.
3 IEA, Net Zero by 2050, Paris, 2001, **https://www.iea.org/reports/net-zero-by-2050**.
4 IEA, Hydrogen, Paris, 2022, **https://www.iea.org/reports/hydrogen**.
5 B. Zohuri, *Cryogenics and Liquid Hydrogen Storage, Hydrogen Energy*, Springer, 2018, pp. 121–139.
6 H. W. Langmi, *et al.*, Chapter 13 – Hydrogen storage, in *Electrochemical Power Sources: Fundamentals, Systems, and*

Applications, ed. T. Smolinka, J. Garche, Elsevier, 2022, pp. 455–486.
7 S. K. Dewangan, *et al.*, A comprehensive review of the prospects for future hydrogen storage in materials-application and outstanding issues, *Int. J. Energy Res.*, 2022, **46**, 16150–16177.
8 R. Moradi and K. M. Groth, Hydrogen storage and delivery: Review of the state of the art technologies and risk and reliability analysis, *Int. J. Hydrogen Energy*, 2019, **44**, 12254–12269.
9 Y. Huang, *et al.*, A review of high density solid hydrogen storage materials by pyrolysis for promising mobile applications, *Ind. Eng. Chem. Res.*, 2021, **60**, 2737–2771.
10 H. Q. Nguyen and B. Shabani, Review of metal hydride hydrogen storage thermal management for use in the fuel cell systems, *Int. J. Hydrogen Energy*, 2021, **46**, 31699–31726.
11 E. D. Sloan and C. A. Koh, *Clathrate Hydrates of Natural Gases*, Taylor & Francis-CRC Press, Boca Raton, FL, 3rd edn, 2008.
12 H. P. Veluswamy, *et al.*, Hydrogen storage in clathrate hydrates: Current state of the art and future directions, *Appl. Energy*, 2014, **122**, 112–132.
13 A. Gupta, *et al.*, Hydrogen clathrates: Next generation hydrogen storage materials, *Energy Storage Mater.*, 2021, **41**, 69–107.
14 Y. A. Dyadin, *et al.*, Clathrate hydrates of hydrogen and neon, *Mendeleev Commun.*, 1999, **5**, 209–210.
15 W. L. Mao, *et al.*, Hydrogen clusters in clathrate hydrate, *Science*, 2002, **297**, 2247–2249.
16 L. J. Florusse, *et al.*, Stable low-pressure hydrogen clusters stored in a binary clathrate hydrate, *Science*, 2004, **306**, 469–471.
17 E. J. Beckwée, *et al.*, Enabling hydrate-based methane storage under mild operating conditions by periodic mesoporous organosilica nanotubes, *Heliyon*, 2023, **9**, e17662.
18 K. A. Lokshin, *et al.*, Structure and dynamics of hydrogen molecules in the novel clathrate hydrate by high pressure neutron diffraction, *Phys. Rev. Lett.*, 2004, **93**, 125503.
19 T. Saikia, *et al.*, Hydrogen hydrate promoters for gas storage—A review, *Energies*, 2023, **16**, 2667.
20 Y. Zhang, *et al.*, Hydrogen storage as clathrate hydrates in the presence of 1,3-dioxolane as a dual-function promoter, *J. Chem. Eng.*, 2022, **427**, 131771.
21 H. Lee, *et al.*, Tuning clathrate hydrates for hydrogen storage, *Nature*, 2005, **434**, 743–746.
22 T. Sugahara, *et al.*, Increasing hydrogen storage capacity using tetrahydrofuran, *J. Am. Chem. Soc.*, 2009, **131**, 14616–14617.
23 D.-Y. Kim, *et al.*, Tuning clathrate hydrates: Application to hydrogen storage, *Catal. Today*, 2007, **120**, 257–261.
24 D.-Y. Kim, *et al.*, Critical guest concentration and complete tuning pattern appearing in the binary clathrate hydrates, *J. Am. Chem. Soc.*, 2006, **128**, 15360–15361.
25 R. Anderson, *et al.*, Phase relations and binary clathrate hydrate formation in the system H_2-THF-H_2O, *Langmuir*, 2007, **23**, 3440–3444.
26 S. Hashimoto, *et al.*, Thermodynamic Stability of H2 + tetrahydrofuran mixed gas hydrate in nonstoichiometric aqueous solutions, *J. Chem. Eng. Data*, 2007, **52**, 517–520.
27 T. A. Strobel, *et al.*, Molecular hydrogen storage in binary THF−H_2 clathrate hydrates, *J. Phys. Chem. B*, 2006, **110**, 17121–17125.
28 N. I. Papadimitriou, *et al.*, Evaluation of the hydrogen-storage capacity of pure H_2 and binary H_2-THF hydrates with monte carlo simulations, *J. Phys. Chem. C*, 2008, **112**, 10294–10302.
29 H. P. Veluswamy, *et al.*, Influence of cationic and non-ionic surfactants on the kinetics of mixed hydrogen/tetrahydrofuran hydrates, *Chem. Eng. Sci.*, 2015, **132**, 186–199.
30 A. Lokshin and Y. Zhao, Fast synthesis method and phase diagram of hydrogen clathrate hydrate, *Appl. Phys. Lett.*, 2006, **88**, 131909.
31 S. Alavi and J. A. Ripmeester, Hydrogen-gas migration through clathrate hydrate cages, *Angew. Chem., Int. Ed.*, 2007, **46**, 6102–6105.
32 P. Englezos, Nucleation and growth of gas hydrate crystals in relation to kinetic inhibition, *Rev. Inst. Fr. Pet.*, 1996, **51**, 789.
33 F. Rossi, *et al.*, Investigation on a novel reactor for gas hydrate production, *Appl. Energy*, 2012, **99**, 167–172.
34 W. Lee, *et al.*, Rapid formation of hydrogen-enriched hydrocarbon gas hydrates under static conditions, *ACS Sustainable Chem. Eng.*, 2021, **9**, 8414–8424.
35 A. Talyzin, Feasibility of H_2–THF–H_2O clathrate hydrates for hydrogen storage applications, *Int. J. Hydrogen Energy*, 2008, **33**, 111–115.
36 T. Tsuda, *et al.*, Storage capacity of hydrogen in tetrahydrothiophene and furan clathrate hydrates, *Chem. Eng. Sci.*, 2009, **64**, 4150–4154.
37 S. Chen, *et al.*, Rapid and high hydrogen storage in epoxycyclopentane hydrate at moderate pressure, *Energy*, 2023, **268**, 126638.
38 K. Ogata, *et al.*, Storage capacity of hydrogen in tetrahydrofuran hydrate, *Chem. Eng. Sci.*, 2008, **63**, 5714–5718.
39 J. Farrando-Perez, *et al.*, Rapid and efficient hydrogen clathrate hydrate formation in confined nanospace, *Nature*, 2022, **13**, 5953.
40 D. Saha and S. Deng, Accelerated Formation of THF-H_2 Clathrate Hydrate in Porous Media, *Langmuir*, 2010, **26**, 8414–8418.
41 F. Su, *et al.*, Rapid and reversible hydrogen storage in clathrate hydrates using emulsion-templated polymers, *Adv. Mater.*, 2008, **20**, 2663–2666.
42 D. Saha and S. Deng, Enhanced hydrogen adsorption in ordered mesoporous carbon through clathrate formation, *Int. J. Hydrogen Energy*, 2009, **34**, 8583–8588.
43 F. Su, *et al.*, Reversible hydrogen storage in hydrogel clathrate hydrates, *Adv. Mater.*, 2009, **21**, 2382–2386.
44 E. J. Beckwée, *et al.*, Structure I methane hydrate confined in C8-grafted SBA-15: A highly efficient storage system

enabling ultrafast methane loading and unloading, *Appl. Energy*, 2024, **353**, 122120.
45 G. Watson, *et al.*, Engineering of hollow periodic mesoporous organosilica nanorods for augmented hydrogen clathrate formation, *J. Mater. Chem. A*, 2023, **11**, 26265–26276.
46 E. Breynaert, *et al.*, Water as a tuneable solvent: a perspective, *Chem. Soc. Rev.*, 2020, **49**, 2557–2569.
47 D. Bai, *et al.*, How properties of solid surfaces modulate the nucleation of gas hydrate, *Sci. Rep.*, 2015, **5**, 12747.
48 J. L. Wang, *et al.*, Use of hydrophobic particles as kinetic promoters for gas hydrate formation, *J. Chem. Eng. Data*, 2015, **60**, 383–388.
49 L. Wang, *et al.*, A review of the effect of porous media on gas hydrate formation, *ACS Omega*, 2022, **7**, 33666–33679.
50 N. N. Nguyen and A. V. Nguyen, "Nanoreactors" for boosting gas hydrate formation toward energy storage applications, *ACS Nano*, 2022, **16**, 11504–11515.
51 H. Li and L. Wang, Hydrophobized particles can accelerate nucleation of clathrate hydrates, *Fuel*, 2015, **140**, 440–445.
52 J. Miyawaki, *et al.*, Macroscopic evidence of enhanced formation of methane nanohydrates in hydrophobic nanospaces, *J. Phys. Chem. B*, 1998, **102**, 2187–2192.
53 N. N. Nguyen and A. V. Nguyen, Hydrophobic effect on gas hydrate formation in the presence of additives, *Energy Fuels*, 2017, **31**, 10311–10323.
54 N. N. Nguyen, *et al.*, Interfacial gas enrichment at hydrophobic surfaces and the origin of promotion of gas hydrate formation by hydrophobic solid particles, *J. Phys. Chem. C*, 2017, **121**, 3830–3840.
55 N. N. Nguyen, *et al.*, Critical Review on Gas Hydrate Formation at Solid Surfaces and in Confined Spaces-Why and How Does Interfacial Regime Matter?, *Energy Fuels*, 2020, **34**, 6751–6760.
56 Z. Li and R.-H. Yoon, Thermodynamics of hydrophobic interaction between silica surfaces coated with octadecyltrichlorosilane, *J. Colloid Interface Sci.*, 2013, **392**, 369–375.
57 M. E. Casco, *et al.*, Experimental evidence of confined methane hydrate in hydrophilic and hydrophobic model carbons, *J. Phys. Chem. C*, 2019, **123**, 24071–24079.
58 M. E. Casco, *et al.*, Methane hydrate formation in confined nanospace can surpass nature, *Nat. Commun.*, 2015, **6**, 6432.
59 M. S. P. Sansom and P. C. Biggin, Water at the nanoscale, *Nature*, 2001, **414**, 157–159.
60 P. G. M. Mileo, *et al.*, Interfacial study of clathrates confined in reversed silica pores, *J. Mater. Chem. A*, 2021, **9**, 21835–21844.
61 V. Meynen, *et al.*, Verified syntheses of mesoporous materials, *Microporous Mesoporous Mater.*, 2009, **125**, 170–223.
62 T. Yasmin and K. Müller, Synthesis and characterization of surface modified SBA-15 silica materials and their application in chromatography, *ACS Sustainable Chem. Eng.*, 2011, **1218**, 6464–6475.
63 J. G. V. Dijck, *et al.*, The interaction of water with organophosphonic acid surface modified titania: An in-depth in-situ DRIFT study, *Surf. Interfaces*, 2020, **21**, 100710.
64 N. B. Kummamuru, *et al.*, Accelerated methane storage in clathrate hydrates using mesoporous (Organo-) silica materials, *Fuel*, 2023, **354**, 129403.
65 N. B. Kummamuru, *et al.*, Experimental investigation of methane hydrate formation in the presence of metallic packing, *Fuel*, 2022, **323**, 124269.
66 E. W. Lemmon, *et al.*, Revised standardized equation for hydrogen gas densities for fuel consumption applications, *J. Res. Natl. Inst. Stand. Technol.*, 2008, **113**, 341–350.
67 H. P. Veluswamy and P. Linga, Macroscopic kinetics of hydrate formation of mixed hydrates of hydrogen/tetrahydrofuran for hydrogen storage, *Int. J. Hydrogen Energy*, 2013, **38**, 4587–4596.
68 *NIST Standard Reference Database, Fundamental Physical Constants: Avogadro Constant*, U. S. A, 2018.
69 T. Kawamura, *et al.*, Enclathration of hydrogen by organic-compound clathrate hydrates, *Chem. Eng. Sci.*, 2011, **66**, 2417–2420.
70 M. Houlleberghs, *et al.*, Building a Cost-Efficient High-Pressure Cell for Online High-Field NMR and MRI Using Standard Static Probe Heads: An *In Situ* Demonstration on Clathrate Hydrate Formation, *Anal. Chem.*, 2023, **95**, 16936–16942.
71 D. Massiot, *et al.*, Modelling one- and two-dimensional solid-state NMR spectra, *Magn. Reson. Chem.*, 2002, **40**, 70–76.
72 M. Avrami, Kinetics of phase change. i general theory, *J. Chem. Phys.*, 1939, **7**, 1103.
73 M. Avrami, Kinetics of phase change. ii transformation-time relations for random distribution of nuclei, *J. Chem. Phys.*, 1940, **8**, 212.
74 M. Fanfoni and M. Tomellini, The Johnson-Mehl-Avrami-Kohnogorov model: A brief review, *Il Nuovo Cimento D*, 1998, **20**, 1171–1182.
75 A. Kumar, *et al.*, Crystallization kinetics for carbon dioxide gas hydrate in fixed bed and stirred tank reactor, *Korean J. Chem. Eng.*, 2016, **33**, 1922–1930.
76 I. L. Moudrakovski, *et al.*, Nucleation and growth of hydrates on ice surfaces: new insights from 129xe nmr experiments with hyperpolarized xenon, *J. Phys. Chem. B*, 2001, **105**, 12338–12347.
77 M. Luzi, *et al.*, Systematic kinetic studies on mixed gas hydrates by Raman spectroscopy and powder X-ray diffraction, *J. Chem. Thermodyn.*, 2012, **48**, 28–35.
78 P. S. R. Prasad, *et al.*, Enhanced methane gas storage in the form of hydrates: role of the confined water molecules in silica powders, *RSC Adv.*, 2020, **10**, 17795–17804.
79 A. Nambiar, *et al.*, CO_2 capture using the clathrate hydrate process employing cellulose foam as a porous media, *Can. J. Chem.*, 2015, **93**, 1–7.
80 J. Zhao, *et al.*, Combined replacement and depressurization methane hydrate recovery method, *Energy Explor. Exploit.*, 2016, **34**, 129–139.

81 J. Zhao, *et al.*, Growth kinetics and gas diffusion in formation of gas hydrates from ice, *J. Phys. Chem. C*, 2020, **124**, 12999–13007.
82 H. Liang, *et al.*, Characterizing mass-transfer mechanism during gas hydrate formation from water droplets, *Chem. Eng. J.*, 2022, **428**, 132626.
83 J. N. Hay, Secondary crystallization kinetics, *Polym. Cryst.*, 2018, **1**, e10007.
84 O. Aktas, *et al.*, Structural variations of MCF and SBA-15-like mesoporous materials as a result of differences in synthesis solution pH, *Mater. Chem. Phys.*, 2011, **131**, 151–159.
85 X.-M. Wang, *et al.*, Direct synthesis and characterization of phenyl-functionalized SBA-15, *Appl. Surf. Sci.*, 2008, **254**, 3753–3757.
86 C. Yu, *et al.*, Study on the dissociation characteristics of methane hydrate in clayey silts, *Chem. Eng. Sci.*, 2022, **252**, 117508.
87 R. Anderson, *et al.*, Gas hydrate growth and dissociation in narrow pore networks: capillary inhibition and hysteresis phenomena, *Sediment-Hosted Gas Hydrates: New Insights on Natural and Synthetic Systems*, The Geological Society, London, 2009.
88 T. Yagasaki, *et al.*, Mechanism of Slow Crystal Growth of Tetrahydrofuran Clathrate Hydrate, *J. Phys. Chem. C*, 2016, **120**, 3305–3313.
89 K. Inkong, *et al.*, Effects of temperature and pressure on the methane hydrate formation with the presence of tetrahydrofuran (THF) as a promoter in an unstirred tank reactor, *Fuel*, 2019, **255**, 115705.
90 D. W. Kang, *et al.*, Confined tetrahydrofuran in a superabsorbent polymer for sustainable methane storage in clathrate hydrates, *Chem. Eng. J.*, 2021, **411**, 128512.
91 H. Tian and Z. Zhang, Revealing the Growth of H_2 + THF Binary Hydrate through Molecular Simulations, *Energy Fuels*, 2020, **34**, 15004–15010.
92 B. Liu, *et al.*, Effect of the Temperature and Tetrahydrofuran (THF) Concentration on THF Hydrate Formation in Aqueous Solution, *Energy Fuels*, 2022, **36**, 10642–10651.
93 R. Ma, *et al.*, Molecular Insights into Cage Occupancy of Hydrogen Hydrate: A Computational Study, *Processes*, 2019, **7**, 699.
94 V. V. Koryakina and E. Y. Shitz, *Condensed Matter and Interphases 22 (Usage of the Kolmogorov–Johnson–Mehl–Avrami Model for the Study of the Kinetics of the Formation of Natural Gas Hydrate in Inverse Oil Emulsions)*, 2020, 327–335.
95 R. Susilo, *et al.*, Methane conversion rate into structure H hydrate crystals from Ic, *AIChE J.*, 2007, **53**, 2451–2460.
96 B. L. L. D. Silva, *et al.*, Sodium alginate polymer as a kinetic inhibitor of methane hydrate formation, *J. Mater. Res. Technol.*, 2021, **12**, 1999–2010.
97 A. A. Aziz, *et al.*, The effect of a secondary process on polymer crystallization kinetics – 3. Co-poly (lactic acid), *Eur. Polym. J.*, 2017, **94**, 311–321.
98 K. Phillipson, *et al.*, The effect of a secondary process on crystallization kinetics – Poly (ε-caprolactone) revisited, *Eur. Polym. J.*, 2016, **84**, 708–714.
99 Y. Nagai, *et al.*, Binary hydrogen–tetrahydrofuran clathrate hydrate formation kinetics and models, *AIChE J.*, 2008, **54**, 3007–3016.
100 H. Yoshioka, *et al.*, Decomposition Kinetics and Recycle of Binary Hydrogen-Tetrahydrofuran Clathrate Hydrate, *AIChE J.*, 2011, **57**, 265–272.
101 J.-H. Yoon, *et al.*, Spectroscopic identification, thermodynamic stability and molecular composition of hydrogen and 1,4-dioxane binary clathrate hydrate, *J. Phys. Chem. Solids*, 2008, **69**, 1432–1435.
102 H. P. Veluswamy, *et al.*, Clathrate hydrates for hydrogen storage: The impact of tetrahydrofuran, tetra-*n*-butylammonium bromide and cyclopentane as promoters on the macroscopic kinetics, *Int. J. Hydrogen Energy*, 2014, **39**, 16234–16243.

